

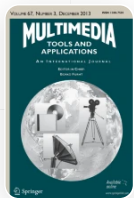
Classification of complex environments using pixel level fusion of satellite data

Published: 19 May 2020

Volume 79, pages 34737–34769, (2020) [Cite this article](#)

[Download PDF](#) ↓


Access provided by Dr. Babasaheb Ambedkar Marathwada University, Aurangabad



[Multimedia Tools and Applications](#)

[Aims and scope](#)

[Submit manuscript](#)

[Amol D. Vibhute](#) , [Karbhari V. Kale](#), [Sandeep V. Gaikwad](#), [Rajesh K. Dhumal](#), [Ajay D. Nagne](#), [Amarsinh B. Varpe](#), [Dhananjay B. Nalawade](#) & [Suresh C. Mehrotra](#)

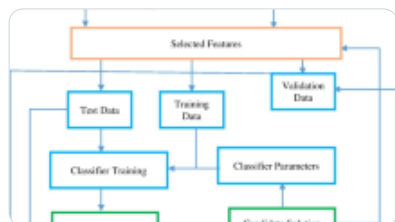
 427 Accesses  10 Citations [Explore all metrics](#) →

Abstract

The present study reports classification and analysis of composite land features using fusion images obtained by fusing two original hyperspectral and multispectral datasets. The high spatial-spectral resolution, multi-instrument and multi-period satellite images were used for fusion. Three pixel level fusion based techniques, Color Normalized Spectral Sharpening (CNSS), Principal Component Spectral Sharpening Transform (PCSST) and Gram-Schmidt Transform (GST), were implemented on the datasets. Performance evaluations of three fusion algorithms were done using classification results. The Support Vector Machine (SVM) and Gaussian Maximum Likelihood Classification (MLC) were used for classification using five types of images, viz. hyperspectral, multispectral and three fused images. Number of classes considered was eight. Sufficient number of ground field data for each class has also

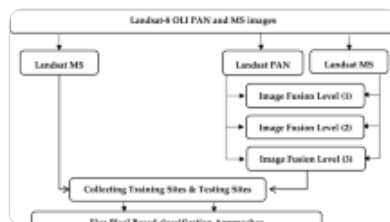
been acquired which was needed for supervise based classification. The accuracy was improved from 74.44 to 97.65% when the fused images were considered with SVM classifier. Similarly, the results were improved from 69.25 to 94.61% with original and fused data using MLC classifier. The fusion image technique was found to be superior to the single original image and the SVM is better than the MLC method.

Similar content being viewed by others



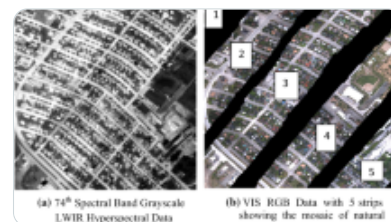
Hyperspectral and LiDAR data fusion in features based classification

Article | 04 December 2021



Fusion Methods and Multi-classifiers to Improve Land Cover Estimation Using Remote Sensing Analysis

Article | Open access
05 June 2021



Comparative Analysis of SVM and ANN Classifiers using Multilevel Fusion of Multi-Sensor Data in Urba...

Article | 09 March 2020

[Use our pre-submission checklist →](#)

Avoid common mistakes on your manuscript.



1 Introduction

Presently diverse sensors have been used for earth observation to identify and classify various patterns on the earth surface. Each sensor has its own spatial and spectral attributes in hyperspectral, multispectral and panchromatic (PAN) images [11], elevation in Light Detection And Ranging (LiDAR) data, amplitude and phase in Synthetic Aperture Radar (SAR) systems. However, analysis of satellite images are still challenging task due to assorted effect of various objects [9]. The heterogeneous and composite terrestrial patterns makes difficult for single source remotely sensed images to meet all requirements of land classification. Nevertheless, detection and classification of heterogeneous-assorted terrestrial patterns is useful application for urban land use/cover classification [28, 30], classification of complex forest areas [8], multiple crop classification [10], etc.

The single source technology and low spatial-spectral data do not provide the details of heterogeneous and assorted earth surface objects. The satellite image analysis is necessary for classification. Accordingly, satellite image fusion is promising way for classification of complex features for near real time applications like urban land classification [5, 6, 9, 30, 42], multiple crop classification [10] and forest area classification [8]. Satellite remote sensing technology is relevant and widely used by remote sensing community for numerous applications and has the potential to offer timely and synoptic information about earth surface features [28].

The single band image provides the high spatial and lower spectral information. The high spectral information is found to be more in multiband data, but spatial related information is low. Hyperspectral data has more spectral channels which give more spectral information about earth surface features [6]. Though, merely PAN, multispectral or hyperspectral data is not sufficient for the purpose [9, 12]. The high spatial and spectral information images are required to overcome the limitations of using only single sensor images [5, 6, 42]. Consequently, a new combined high spatial and spectral resolution image approach is achieved through fusion of images.

Fusion of images is generally carried out by three different approaches, (i) pixel or iconic level, (ii) feature level and (iii) decision or knowledge level [3, 34]. These approaches are used as per applications. The fusion approach based on pixel level enhances efficiency of classification and detection [34]. Popular methods based on pixel level fusion algorithms are wavelet transform, GST, PCSST and CNSS or Brovey transform etc. generally used for enhancing the accuracy of classification. The statistical methods for classification used are SVM [12, 14, 28] and MLC [1, 28, 36] which have been extensively used due to their efficiency and simplicity. The genetic algorithm alone or combined with SVM has also been used and found to be better than SVM and MLC as classifier [40, 41].

However, earlier studies focus on the fusion of either hyperspectral and LiDAR data, or hyperspectral and PAN data, or PAN and multispectral datasets. Some studies have been also reported based on fusion of multispectral and hyperspectral images [37]. However, fusion on hyperspectral and multispectral images were not studied sufficiently enough to access its usefulness for various types of applications like classification of complex objects. Therefore, the present work aims to use the fusion approach for classification of complex-mixed land objects. The fusion framework of Hyperion and LISS-IV satellite images is carried out with multi-temporal data to get fusion images which have overcome limitations of single sensor and single low resolution images.

In the present manuscript, high spatial resolution IRS-Linear Imaging Self Scanner (LISS)-IV (multispectral) image with high spectral resolution EO-1 Hyperion hyperspectral image have been utilized for getting joint high spatial and spectral resolution images. The main objectives were to

classify the terrestrial patterns by original and fused datasets and to evaluate the performance of fusion and classification methods. In the present study we have carried out: (1) Fusion of LISS-IV and Hyperion images in three techniques using CNSS, PCSST and GST, (2) acquiring sufficient number of data at field level to be used for supervised classification, (3) applying and analyzing results obtained through the MLC and SVM methods to original images as well as fused images for classification of the Area of interest (AOI) which was assumed to be having eight different types of objects.

Details of this study are presented in six sections. This section one has given background of the study, originality of the paper, and set objectives for the present study. The section 2 contains brief description of related work reported in the literature and motivation of the present work. The section 3 provides details of AOI, information regarding relevant satellite images and method of acquiring field data. The section 4 contains the methodology used in the study. It consists of four steps i.e. preprocessing, image fusion, digital image classification and evaluation of accuracy of classifiers. The section 5 has provided details of classifications using MLC and SVM methods which consist of preprocessing of the datasets, data fusion, training and testing. The section also contains details regarding results and comparison of two methods with reference to original and fused images. The last section summarizes with conclusion and future scope.

2 Literature retrospect

In contrast to traditional satellite image fusion, numerous investigators reported study of image fusion using only on PAN with multi or hyperspectral images along with various methods for classification of the earth surface features [28].

Zoleikani et al. (2017) [42] have used Hyperion and IRS-PAN data for image fusion for mapping of urban land cover. The study revealed the image fusion by pixel and object based classification methods and received good accuracy of classification. The urban land cover classification was done (Rajput et al. (2017)) [30] using fusion of very high resolution World View-2 PAN and multispectral data and compared the image fusion methods such as Hue-Saturation-Intensity, Brovey Transform, Principal Components Analysis (PCA), Discrete Wavelet Transform, Stationary Wavelet Transform, Non Sub-sampled contourlet Transform and Pseudo Wigner Distribution (PWD), etc. Instead, Andrejchenko [2] et al. (2019) was studied on decision level fusion for classification of urban and agricultural areas based on probabilistic graphical markov and conditional random fields. The fusion of complementary decision sources such as fractional abundances, obtained by sparse unmixing and probabilistic outputs from a soft classifier were measured through two hyperspectral datasets with limited training samples.

Debes et al. (2014) [9] have studied the supervised and unsupervised approaches with graph-based method for the classification of land patterns using hyperspectral and LiDAR data. The fusion of data was carried out using spectral-spatial and elevation information. Dalponte et al. (2008) [8] have worked on hyperspectral and LiDAR data for classification of complex forest areas using SVM and MLC methods. They found that SVM is better for multisource data. Swatantran et al. (2011) [33] have estimated amount of biomass using fusion of structural metrics of LiDAR and spectral characteristics of hyperspectral data in the Sierra Nevada. Abbasi et al. (2015) [1] have carried out fusion of LiDAR and hyperspectral data for the classification of surface objects especially urban areas based on Naïve Bayes classifier with decision level fusion. They have also performed dimensionality reduction using PCA and Minimum Noise Fraction (MNF) methods, measurement of texture features based on GLCM (Grey Level Co-occurrence Matrix) and classification using MLC method. They have achieved satisfactory results. Similarly, Man et al. (2015) [28] have used hyperspectral and LiDAR data for urban land-use classification based on pixel and feature-level fusion. The study shows use of LiDAR data for the extraction of intensity and height information using classification based on SVM, MLC with object oriented classifiers.

Unlike LiDAR and hyperspectral data, PAN and multispectral data have capacity of providing high spatial resolution images which can be utilized for classification of earth surface features using spatial features. Additionally, classification of urban area and vegetation was carried out by Kumar et al. (2015) [24] using both multispectral images of the Landsat-5 Thematic Mapper image along with WorldView-2 image with spatial resolutions 30 m and 2 m respectively. The trafficability assessment was done by decision level fusion on hyperspectral and SAR data [7] using supervised classifiers. Kosaka et al. (2005) [23] classified forest using the fusion of PAN and multispectral images with object based classification method. Moreover, Ashraf et al. (2012) [3] worked on freshwater land-cover mapping using QuickBird image fusion.

Several researchers have reported various types of study related to fusion and classification for urban land. Zoleikani et al. (2017) [42] compared pixel based (SVM) and object based classifications for land-cover mapping in an urban area. The GST, PCT, Haar wavelet, and À Trous Wavelet Transform (ATWT) fusion algorithms have also been used and classification accuracy was evaluated. Ehlers et al. (2010) [11] used series of multi-date multispectral and PAN Ikonos image and a Terra SAR-X radar image for assessing the quality of pan sharpening fusion methods.

However, these studies do not worked on the fusion of hyperspectral and multispectral datasets. Thus, the said issues of literature were investigated in the present research for obtaining the set objectives. The fusion of multi-temporal, multi-resolution and multi-sensor images provides additional spatial and spectral information. This task is very critical and challenging which is needed to study varied

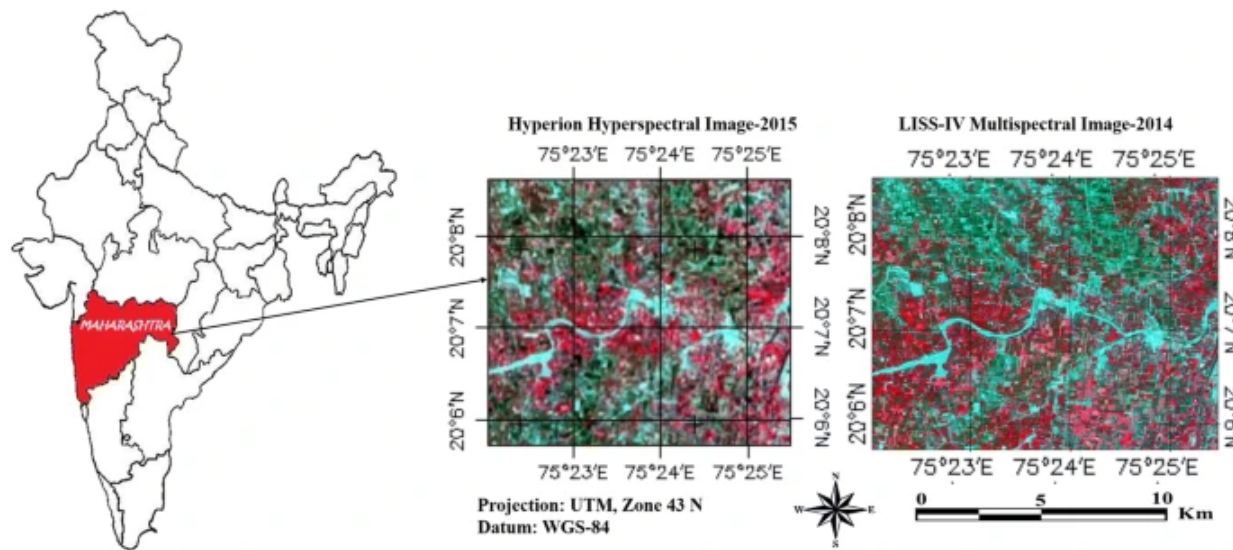
properties of earth surface. Therefore, several limitations of the earlier studies were selected and get motivated to achieve the goal.

3 Area of interest (AOI) and used datasets

3.1 Area of interest (AOI)

The AOI is the composite-assorted terrestrial scene with hilly region and some farming and urban areas of Aurangabad district of Maharashtra, India (Fig. 1). It covers approximately 32.04 km² land, geographically extending from 1928'43.27" - 2024'52.19"N latitude and 7513'10.75" -7530'14.87" E longitude with an average altitude of 568 m above the sea level [37]. The landscape of the study area is uneven and the spatial reference is Universal Transverse Mercator (UTM) zone 43 North and World Geodetic System (WGS)-84 datum.

Fig. 1



The geo-location of the study area and its corresponding Hyperion and LISS-IV images

The study of this region is a challenging task. Difficulties may be due to various factors like (1) spectral and spatial similarity between vegetation, buildings, barren lands, roads and rivers lots leads to misclassification, (2) difficulty in analysis of multi-date and multi-sensor data, (3) mixed pixel effects, (4) atmospheric correction and hyperspectral data dimensionality reduction issue, and (5) field information and its variation.

3.2 Datasets

The fusion is done by two datasets for the present study viz. Hyperion and LISS-IV data. The hyperspectral data is obtained by USGS-NASA [17] and multispectral data is obtained by NRSC-ISRO, India via Earth Observing-1 (EO-1) Hyperion and IRS-P6 Resourcesat-II (satellite revisit period is of 5 days) LISS-IV sensors respectively. The thematic maps were prepared through Survey of India (SOI) toposheet at 1:50,000 scales. Global Positioning System (GPS) was used to capture the ground truth points (GTP).

3.2.1 Hyperspectral data

The Hyperion data contains 242 spectral bands ranging from 355.59–2577.08 nm in the visible (35 bands), near infrared (35 bands) and shortwave infrared (172 bands) of date 21 March, 2015 was used. The spatial and spectral resolutions were 30 m and 10 nm (continuous spectral coverage) respectively, with 7.74 km by 100 km swat per image. The USGS have provided the level 1 T orthorectified image (Level 1 T (GeoTIFF)) in band sequential (BSQ) format. The EO-1 satellite (temporal resolution is 200 days) was over-passed the studied region on 21 March, 2015 through the 147/146 orbit path/target path and 46/46 orbit row/target row [35]. Some of the important parameters are provided in Table 1.

Table 1 Some important Parameters of Hyperion and LISS-IV Data

3.2.2 Multispectral data

The LISS-IV multispectral data was acquired on February 21, 2014, between the times 14:15 and 14:18 h. The spatial resolution is high in LISS-IV data of 5.8 m with 23.5 swaths per scene. The spectral bands are found to be three in LISS-IV data ranging from 520 to 860 nm of Green, Red and Near Infrared (NIR). Subsequently, all three spectral bands were fused with visible to NIR region of hyperspectral image. In our proposed approach, an amount of 38 spectral bands of Hyperion data were fused with three spectral bands of LISS-IV data.

3.2.3 Field campaign

The GPS of Android Smartphone was used to collect the GTPs through field campaign during the period of February 10, 2015 to March 25, 2015 in between 0800 to 1330 h (IST) with clear environmental conditions. The observed field sites were captured using digital cameras. Concurrently, discussions were done with local people and noted on digital notebooks for verifying the field sites. The digital conversion was made of collected GTPs and proximal sensing data. Moreover, the GTPs were transferred to region of interests (ROIs) on the co-registered Hyperion and LISS-IV data and used for

development of the training and testing sets. The verification and validation of used data was frequently evaluated using Google map and Google earth.

4 Architecture of the proposed methodology

The proposed methodology is divided into four sections i.e. preprocessing, image fusion, digital image classification and evaluation of accuracy of classifiers.

4.1 Pre-processing of satellite images

The data was pre-processed to correct the raw images, remove the unwanted noise and diminish the dimensionality using relevant algorithms. Subsequently, the geographic coordinates were set according to the size of study area as upper left was 200,945.47 N and 752,122.44 E, whereas lower right was 200,514.54 N and 752,624.19 E. The LISS-IV image was already corrected by the providers. However, an orthorectification [22] was made on both the transferred images. Further processing was carried out on the preprocessed LISS-IV data as this data needs merely that much preprocessing. The image was converted to the reflectance and spatial subset was designed using ROIs. The implementation of fusion and classification algorithms was done on preprocessed data. The data processing was carried out through Environment for Visualizing Images (ENVI) 5.1 image processing software and ArcGIS 10.0 software. The acquired images were from different sources and satellite platforms. Hence in preprocessing we brought them in to same projection and geographic coordinate system [22].

In the case of hyperspectral data, firstly, the raw image (GeoTIFF format) was transferred to the ENVI standard format using 'Hyperion Tools'. Secondly, orthorectification was done and identified overlapped and uncalibrated water vapor bands [35]. As a result, total 87 bands were identified as a bad and water vapor bands which were eliminated from further processing. The Hyperion data was also converted to reflectance to identify the characteristics of spectral features [35]. Lastly, atmospheric correction was done on the original hyperspectral bands using the QUAC algorithm in ENVI 5.1 software [35]. The QUAC algorithm [35] was implemented using Eq. 1.

$$\rho = \left(\rho_1 + \rho_2 + \dots + \rho_n \right) / n$$

(1)

where, ρ are the end member spectrum of the surface and the average reflectance of different materials, and n specifies the end member number.

After the atmospheric correction, the Hyperion image was processed using MNF method to diminish the dimensionality and systematic noise caused by sensor and processing anomalies during image analysis [27, 28]. The MNF method has been used as a linear transformation modified with PC transform [27].

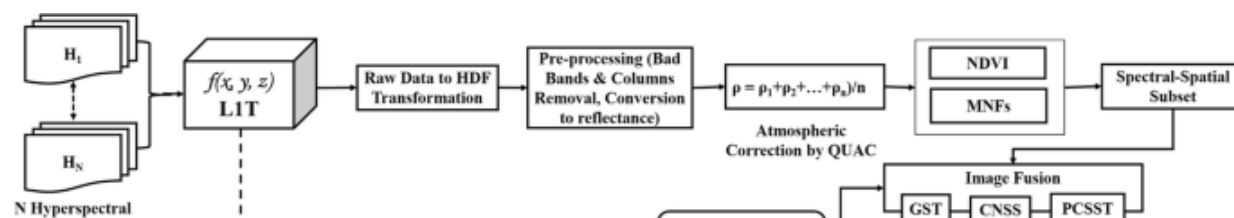
The spectral subset of Hyperion data was generated according to the wavelength range of LISS-IV image. The LISS-IV image has three spectral channels ranging from 520 to 860 nm [16]. Thus, thirty five spectral channels of Hyperion MNF image was used for fusion and rest of the 120 bands were skipped from the further processing. Utilized bands from the Hyperion MNF image was ranging from 518.39–864.35 nm with 35 bands. The pixel size of fused images was 5.8 m × 5.8 m. The original preprocessed Hyperion and LISS-IV images are given in Fig. 1.

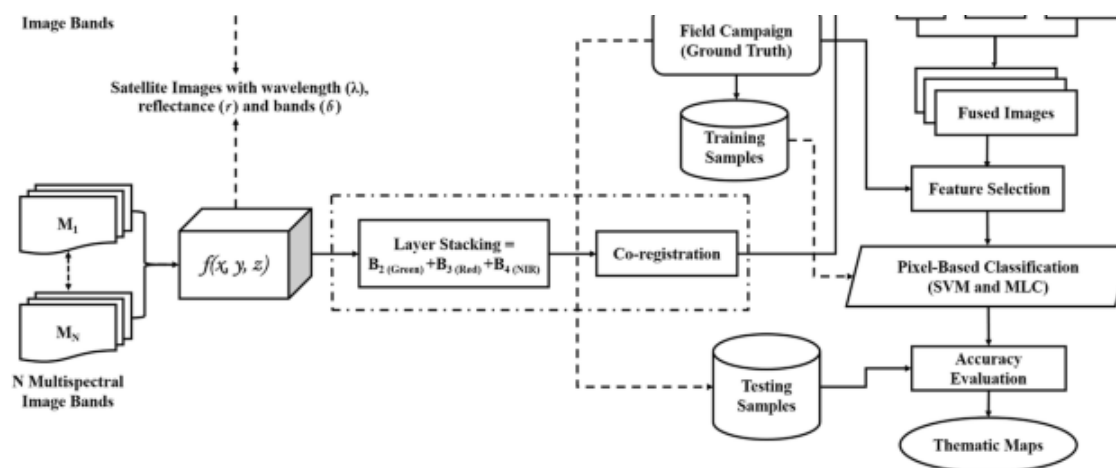
4.2 Satellite image fusion framework

Fusion of Satellite image can be made by combination of two or more images into a new fused image using some fusion techniques [3]. Applicability of the fusion of satellite images are varied as per its applications, complexity of the problem and variety of data types. Moreover, image fusion is carried out for better visual interpretation though the amalgamation of image modalities or various spectral uniqueness [34]. The fusion can be classified into three levels (Pixel, Feature and Decision) based on the step at which image fusion happens. (1) Pixel-based image fusion highlights the original information available in the various images which afford subtle information and performed at the raw images after co-registration. (2) Feature-level fusion is processed through feature extraction for producing unknown features and mostly used for data compression. (3) Decision-level fusion is processed on separate images and merely final results are fused for decision making [28].

In this work, our aim was to enhance the classification efficiency and detection methods. Therefore we have only considered pixel-level image fusion strategy [34]. The three different methods using pixel-level have given similar results (See Fig. 15). Results obtained by CNSS fused image have found to be better than corresponding results. In the present paper, pixel based image fusion approach is implemented on the datasets for land cover classification. The Fig. 2 shows the flowchart of proposed architecture of the developed fusion and classification framework.

Fig. 2





Flowchart of the proposed methodology

Three pixel based methods of image fusion viz. GST, PCSST and CNSS have been used in the present study. The spatial and spectral information was extracted from the complex features after the image fusion. Therefore, both the datasets were converted to their appropriate format. The preprocessed images were used for fusion and classification.

4.2.1 Fusion using GST method

The spectral response factor of high resolution image is utilized by the GST method. Meanwhile, GST is applied to fuse the transmitting synthesized high spatial and low spatial resolution image. Firstly, the mean values and high frequency variance of a high spatial resolution image is extracted. Subsequently, the first factor of GST is replaced by the new high resolution image. Lastly, the obtained set is inversely transformed for generating the high resolution image [4, 19, 42]. The GST algorithm was mathematically formulated by Eq. 2.

$$\begin{aligned}
 & \left(\begin{array}{c} HSRI \\ \{ \{ LSRI_1 \} \} \vdots \\ \{ \{ LSRI_N \} \} \end{array} \right) \overset{GST}{\rightarrow} \left(\begin{array}{c} GS_1 \\ \{ \{ GS_2 \} \} \vdots \\ \{ \{ LSRI_{N+1} \} \} \end{array} \right) \overset{\text{operatorname{Re}}}{\text{place}} \{ GS_1 \} \\
 & \{ \underset{\text{with operatorname{mod}}}{\text{ifiedHSRI}} \} \rightarrow \left(\begin{array}{c} MHSRI \\ \{ \{ GS_2 \} \} \vdots \\ \{ \{ LSRI_{N+1} \} \} \end{array} \right) \overset{\text{inverse}}{\text{operatorname{GS T}}} \\
 & \rightarrow \left(\begin{array}{c} X \\ \{ \{ F_1 \} \} \vdots \\ \{ \{ F_N \} \} \end{array} \right) \quad (2)
 \end{aligned}$$

where, *HSRI* is the high spatial resolution synthesized image merge transformed with *LSRI* low spatial resolution images, *MHSPI* is the modified *HSRI* and *F* is the fused images.

The Eq. 3 is implemented for GST method for constructing the synthesized high resolution image.

$$HSRI = \frac{1}{N} \sum_{i=1}^N LSRI_i \uparrow$$

(3)

where, $HSRI$ is the synthesized image (high spatial resolution), $LSRI_{i\uparrow}$ is the up-scaled i -th low spatial resolution image bands and N is the total number of $LSRI$.

4.2.2 Fusion using PCSST method

The PC algorithm is statistically accurate that restores a multivariate dataset of correlated factors into a dataset of uncorrelated linear combinations of the factors. This algorithm produces an uncorrelated feature space of LSRI along with converting the PCs according to the eigenvectors of their compatible covariance matrices. First PCs comprises most of the data variance among all the remaining bands. The HSRI is statistically adjusted to match with the PCs. Subsequently, inverse PC transformation is executed on the obtained new set of PCs and high resolution fused images are generated [4, 20, 42]. The mathematical procedure of PCSST algorithm is given in Eq. 4.

$$\left(\begin{array}{c} LSRI_1 \\ LSRI_2 \\ \vdots \\ LSRI_N \end{array} \right) \overset{PCT}{\rightarrow} \left(\begin{array}{c} PC_1 \\ PC_2 \\ \vdots \\ PC_N \end{array} \right) \overset{\text{Re place } PC_1}{\underset{\text{with } \text{modified HSRI}}{\rightarrow}} \left(\begin{array}{c} MHSRI \\ PC_2 \\ \vdots \\ PC_N \end{array} \right) \overset{\text{inverse}}{\underset{PCT}{\rightarrow}} \left(\begin{array}{c} F_1 \\ F_2 \\ \vdots \\ F_N \end{array} \right)$$

(4)

where, $LSRI$ is the low spatial resolution images, PC is the principal components, $MHSPI$ is the modified $HSRI$ and F is the fused images. The PCT method is implemented by Eq. 5 for fusion of used images.

$$F_i = LSRI_i \uparrow + v_i \left(HSRI - PC1 \right)$$

(5)

where, F_i is the i -th band in fused image, $LSRI_{i\uparrow}$ is the up-scaled i -th low spatial resolution image bands, v_i is the i -th element of most significant eigenvector and $HSRI$ is the high resolution image and $PC1$ is the first PCT of $LSRI$.

4.2.3 Fusion using CNSS method

The modified version of Brovey transform [18] is extended in CNSS algorithm used in multispectral and improved for hyperspectral image sharpening. Concurrently, the CNSS method can be utilized for sharpening any band from the image and preserve the input images original data type with varied range. The provided input image channels are assembled into spectral segments defined by the spectral range of the sharpening channels. The input bands (LSRI) is multiplied by the HSRI sharpening bands and then resulted values are normalized by averaged LSR data over the spectral bands in the segment (covered range of HSRI) [11, 15]. The CNSS algorithm is mathematically calculated using the Eq. 6.

$$F_i = \frac{\left(LSRI_i \times HSRI \right)}{(LSRI)_s}$$

(6)

where, F_i is the sharpened image, $LSRI_i$ is the LSRI band, $(LSRI)_s$ is the band averaged $LSRI$ over the $HSRI$ spectral bands in the segment (covered wavelength range).

4.3 Image classification

4.3.1 Training and testing samples

As per the survey of study area, eight (08) suitable classes were identified. These classes were (1) Residential regions, (2) River sand, (3) Dense vegetation (4) Sparse vegetation, (5) Black soil, (6) Roads, (7) Bare soil and (8) Water. The training and testing samples at ground level for classification were carried out by GTPs, spectral-spatial features and visual information. The Table 2 highlights the details of training and testing samples along with their color codes.

Table 2. Image Classes, Training and Testing Pixels for Multispectral and Hyperspectral Image along with classification color codes of classes.

4.3.2 Pixel-based supervised classification methods

Digital image classification was attempted using two supervised based approaches viz. MLC and SVM. The proposed fusion approach and original satellite images have been classified with advance level statistical algorithms specifically appropriate to analyze the satellite images. In the following section, we briefly recall the key properties of used classification methods for our study.

Maximum Likelihood Classification (MLC) The MLC is one of the well-known and popular statistical

parametric methods used for supervised classification based on Bayes theorem [13, 25, 32]. The pixel with maximum likelihood is classified into particular class. The trainings to the particular spectral signature or the priory probability are used in MLC method. Thus, the misclassification is reduced for each class. According to the Bayes formula, an implementation of MLC method is defined using the posterior probability. Thus, the class of a posterior probability is defined as given in Eq. 7:

$$p(C_j/X) = \frac{p(X/C_j)p(C_j)}{\sum_{j=1}^m p(X/C_j)p(C_j)} \quad (7)$$

where, $p(C_j)$ is the prior probability of class C_j and $p(X/C_j)$ is the conditional probability of observing X from class C_j (probability density function). Thus, the computation of $p(C_j/X)$ is reduced to determination of $p(X/C_j)$. The maximum likelihood function $p(X/C_j)$ can be expressed as given in Eq. 8,

$$p(X/C_j) = \frac{1}{(2\pi)^{n/2} |\Sigma_j|^{0.5}} \exp\left[-\frac{1}{2} (DN - \mu_j)^T \Sigma_j^{-1} (DN - \mu_j)\right] \quad (8)$$

where, $DN = (DN_1, DN_2, \dots, DN_n)^T$ is the vector of pixel with n number of bands $\mu_j = (\mu_{j1}, \mu_{j2}, \dots, \mu_{jn})^T$ is the mean vector of the class C_j and Σ_j is the variance-covariance matrix of class C_j which can be written as given in Eq. 9 [13]:

$$\Sigma_j = \begin{bmatrix} \sigma_{11} & \sigma_{12} & \dots & \sigma_{1n} \\ \sigma_{21} & \sigma_{22} & \dots & \sigma_{2n} \\ \dots & \dots & \dots & \dots \\ \sigma_{n1} & \sigma_{n2} & \dots & \sigma_{nn} \end{bmatrix} \quad (9)$$

Support Vector Machine (SVM) The SVM is the statistical advance supervised machine learning method which is widely used for various applications of remote sensing [12, 14]. The two main reasons behind the use of SVM is: (1) the training samples are required less and its architecture is easy, (2) with less training samples, produces better accuracy [22]. The SVM algorithm is rely on fitting a separating hyperplane which can offer the best separation between two classes in a multidimensional feature space.

In this study, Gaussian Radial Basis Function (RBF) was considered as the kernel function for

identifying suitable hyperplane. The mathematical implementation of RBF is shown in Eq. 10.

Gaussian Radial Basis Function (RBF): $k(x_i, x_j) = \exp(-\gamma \cdot \|x_i - x_j\|^2), \gamma > 0$ (10).

where, γ is the kernel constant parameter.

4.4 Accuracy assessment

The accuracy assessment was done in ENVI 5.1 software. Testing samples acquired from the field campaign were used. Error matrix was used to compute values of overall accuracy (OA), producer's accuracy (PA), user's accuracy (UA) and Kappa statistics [36]. The Kappa (K) is a statistical test that quantifies the accuracy of the classification ranging from -1 to 1 [13]. The columns of error matrix correspond to the reference samples, whereas rows to the classified samples. The diagonal number of the error matrix represents the correctly classified pixels [39]. The OA, PA, UA and K-values are calculated by Eq.s (11), (12), (13) and (14) respectively [13].

$$OA = \frac{\sum_{x=1}^A C_{xx}}{N} \times 100\%$$

(11)

where, N and A is the total number of pixels and classes respectively and C_{xx} is the element of confusion matrix at position x^{th} row and x^{th} column (diagonal values).

$$PA = \frac{C_{xx}}{\sum c} \times 100\%$$

(12)

where, C_{xx} is the element at position x^{th} row and x^{th} column and $\sum c$ is column sums.

$$UA = \frac{\text{C}_{xx}}{\sum r} \times 100\%$$

(13)

$\sum r$ is row sums.

$$k = \frac{\sum_{i=1}^A r_i \left(X_{ii} - \frac{\sum c_i \sum r_i}{N} \right)}{\sum_{i=1}^A r_i \left(\sum c_i \sum r_i \right)}$$

(14)

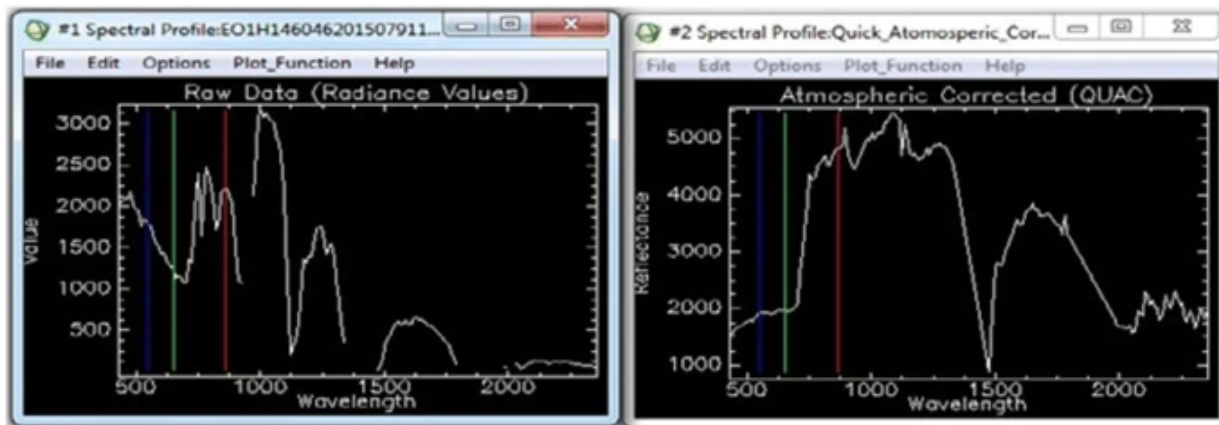
where, k =kappa statistics, r = number of rows and columns in the error matrix, X_{ii} = number of observations in row i and column i , $\sum c_i$ = marginal total of column i , $\sum r_i$ = marginal total of row i , N = total number of observations.

5 Results and discussion

5.1 Preprocessing of the datasets

Original Hyperion image was atmospherically corrected by QUAC algorithm to correct atmospheric effects due to atmosphere [35]. The Fig. 3 shows the spectral profile of vegetation class before and after atmospheric correction.

Fig. 3



Spectral profile of vegetation before and after atmospheric correction (QUAC)

It can be seen from the Fig. 3 that raw data had dominated by radiance values. So it was difficult to extract the classes from the radiance data. When applied QUAC model, the gap between wavebands were converted into reflectance spectra for the whole spectrum. So hyperspectral satellite data classification is not suitable without atmospheric correction.

The vegetation feature was extracted using Normalized Difference Vegetation Index (NDVI) [31] spectral index (Eq. 15) with the fused datasets.

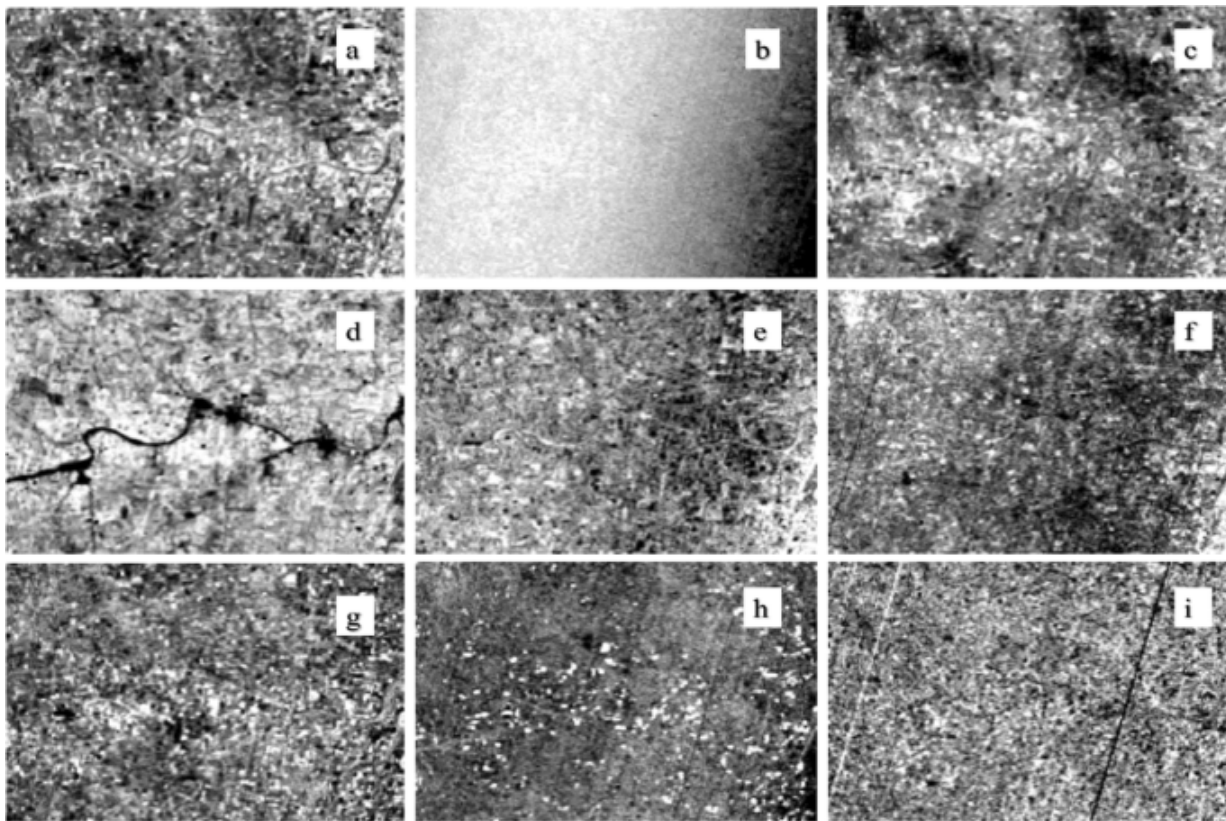
$$NDVI = \frac{\left(R_{864 \text{ nm}} - R_{671 \text{ nm}} \right)}{\left(R_{864 \text{ nm}} + R_{671 \text{ nm}} \right)}$$

(15)

where, R denotes the reflectance at the bands given by the subscripts.

The bright color of Fig. 4a, indicates the vegetation regions. It was verified by the NDVI values with the corresponding field data. The values of NDVI corresponding to these bright areas were found to be more than 0.70. The vegetation regions were correctly extracted from the all images. The MNF 2 and MNF 3 highlighted the residential region, river sand and roads (see Fig. 4c and d). The rest of the MNFs were not used due to their poor performances.

Fig. 4



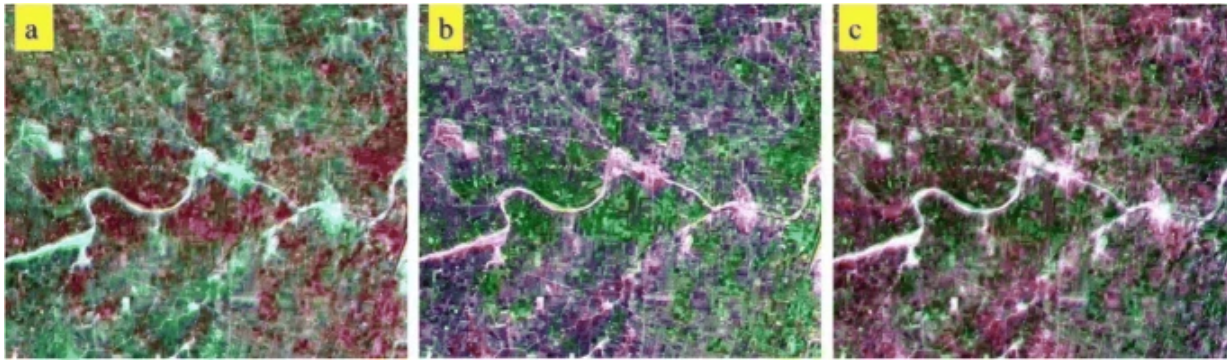
a NDVI, **b** MNF 1, **c** MNF 2, **d** MNF 3, **e** MNF 4, **f** MNF 5, **g** MNF 6, **h** MNF 7 and **i** MNF 8

5.2 Hyperion and LISS-IV data fusion

We have also explored performance of fusion methods and fused data for classification. Three fusion

algorithms, CNSS, GST and PCSST, were implemented. The spectral profiles were generated for each class and compared with original hyperspectral data. The Fig. 5 indicates the output of fused images as obtained by CNSS, GST and PCSST using Hyperion and LISS-IV images.

Fig. 5



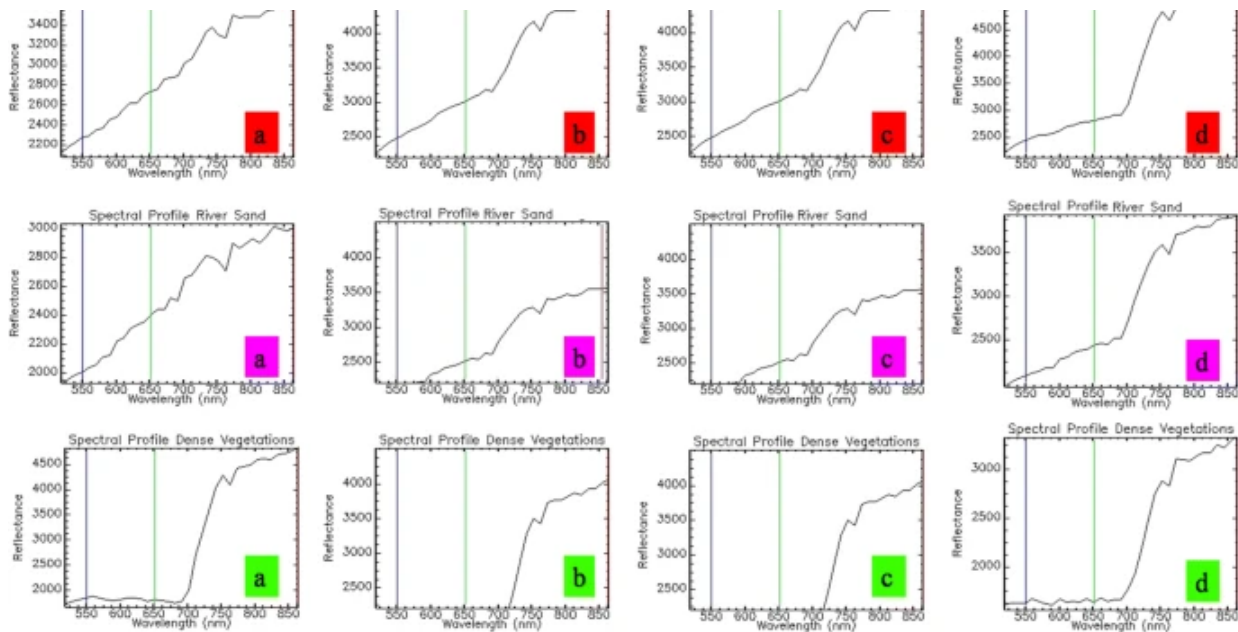
The output of (a) CNSS, (b) GST and (c) PCSST fused images

These fused images were visually interpreted for selecting the appropriate classes. The ROI detection was done using histograms of the image and band thresholding algorithm [21]. As a result, fused images obtained by the CNSS and PCSST appeared to be better as compared to the images computed by the GST. The fused images obtained by the GST have more color variations as compared to the original data, though fused images by the PCSST have provided satisfactory results. On the other hand, Classification results obtained by the CNSS and GST were better.

The spectral profiles were generated for every fused image and compared with original hyperspectral spectra. All the spectral profiles were accurately matched with original spectra. Moreover, spatial information along with spectral information was extracted from the fused images. The Figs. 6, 7 and 8 show the computed spectra for each class. Some classes were slightly affected due to fusion effect. Spectral signatures corresponding to residential class were similar as obtained by the fused and the original images. However, spectra of fused images were slightly lower at wavelength around 700 nm as compared to original data. The river sand and residential class spectra were similar to the PCSST fused image and original data. This is due to similar characteristics of both classes. The spectra corresponding to river sand class were similar as derived from the CNSS and GST.

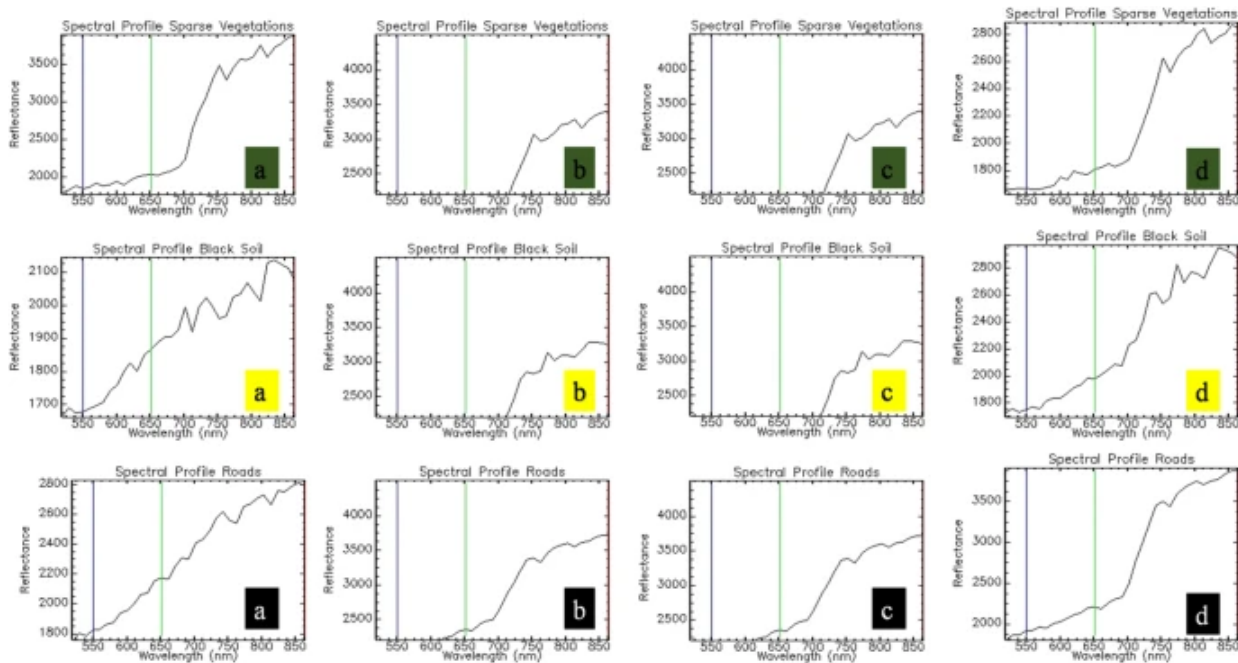
Fig. 6



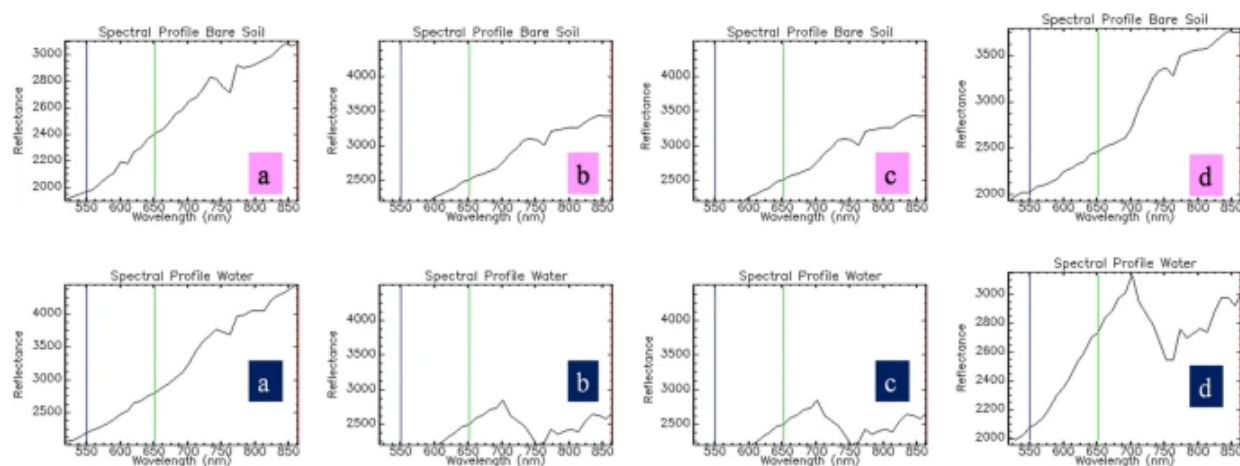


Spectral profiles of (a) original hyperspectral image, (b) CNSS image, (c) GST image and (d) PCSST image for residential region, river sand and dense vegetations respectively

Fig. 7



Spectral profiles of (a) original hyperspectral image, (b) CNSS image, (c) GST image and (d) PCSST image for sparse vegetations, black soil and roads respectively

Fig. 8

Spectral profiles of (a) original hyperspectral image, (b) CNSS image, (c) GST image and (d) PCSST image for bare soil and water respectively

Similarly, values of reflectance corresponding to dense and sparse vegetation have higher values at the NIR region of spectrum. The spectral profile was alike to original and PCSST fused image of dense and sparse vegetations. The CNSS and GST fused images have provided related spectral information for both the vegetation classes. Nonetheless, results obtained by the spectra of sparse vegetation somewhat lower corresponding results from the GST and CNSS methods.

Black soils have various chemical, physical and biological properties and additionally they have different amount of moisture and clay. Due to the reason, one expects to have varied spectra for black soil. The spectral characteristics of black soils may also vary according to the geolocation. However, the spectra of black soil are matched with PCSST fused image. Spectral reflectance of bare soil (original image) obtained by all three fused images were not very different. The spectral information of road class was found to be varied for the fused images. The original hyperspectral and PCSST fused image have produced higher reflectance of road class as expected. Similarly spectra generated through the CNSS and GST fused images were found to be with some variation.

As per the knowledge of visual interpretation, these two methods have produced spectral mixing of other classes. The road class is matched with river sand and residential region due to its similar spectral properties. The water was less during March, 2015 in the studied region. Hence, corresponding spectra of water class was not reliable from the original hyperspectral images. The high reflectance is found to be more in visible region for the water class. Fused images by the PCSST have produced reliable spectra.

The supervised classification techniques, viz. MLC and SVM, were applied using spatial features and spectral profiles derived by original images (Hyperion and LISS-IV), three types of fused images due to CNSS, GST and PCSST algorithms along with data collected at ground level. Details are given in the next section.

5.3 Training and testing samples

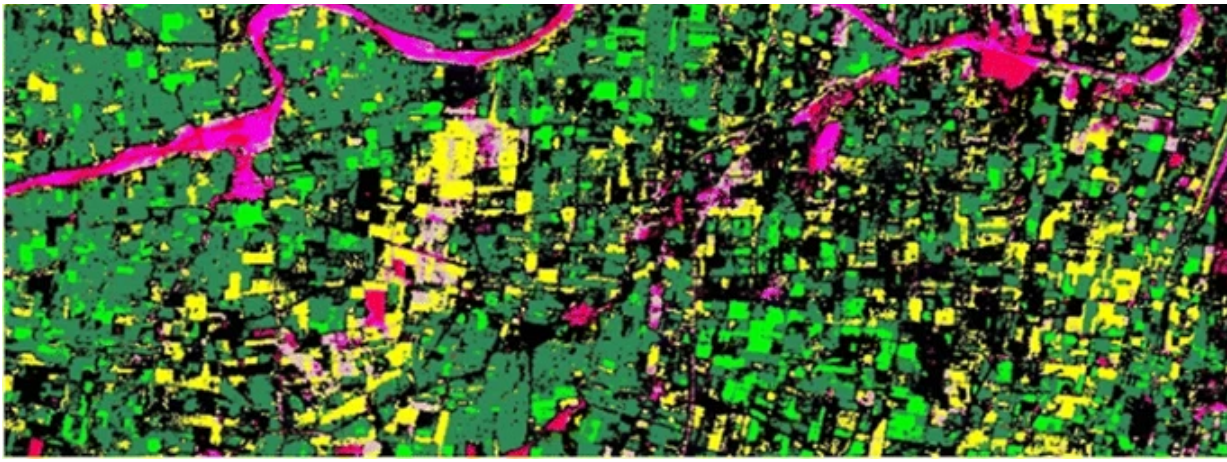
Nearly, 747 and 1253 pixels were identified and randomly selected as samples for training and testing, respectively. Likewise, the hyperspectral and fused datasets were individually trained and tested by 3288 and 4461 random pixels respectively. Selected individual training samples for each class is given in Table 2 for both the datasets and fused images along with their color codes of eight different types of objects. The training and testing samples were derived from the images according to the field campaign, ground reference data, spectral information of each class (Figs. 6, 7 and 8), spatial structure of objects, users knowledge about the satellite image and image patterns (shape, size, standard false composite color, texture, etc.). The separate training-testing pixels were used for LISS-IV data due to dissimilar structures of datasets. However, Hyperion and fused images were trained and tested through similar number of samples (3288 and 4461) acquired at ground level.

5.4 Results of MLC based classification

The original images were individually classified using MLC method. The spectral features were calculated and used for classification of data. The said training samples were inputted to the MLC based supervised method in ENVI 5.1 software. The additional input variables required for the MLC were probability threshold values and data scale factor. Accordingly, probability threshold value for each class was assigned as 0.05 and data scale factor as 1. The resulted output map is illustrated in Fig. 9 for original multispectral data.

Fig. 9





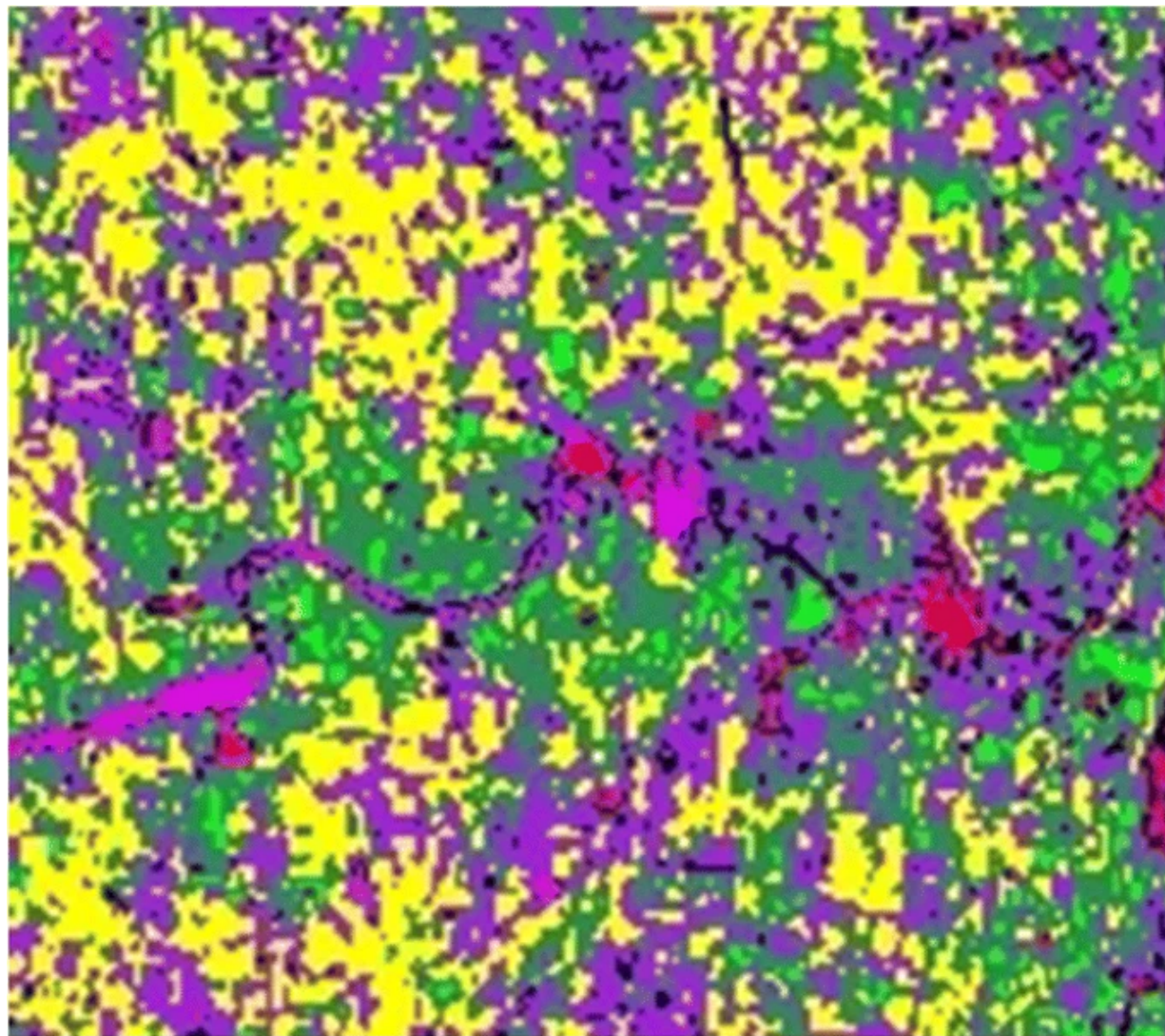
MLC classification output layer of original LISS-IV image

The results indicate that the classes except the class related to road (road class) have been identified accurately. The road class was misclassified with bare soil due to spectral similarity. The accuracy was measured by confusion matrix for the original LISS-IV classification image derived by MLC method. The results corresponding to accuracy assessment with confusion matrix are given in Table 3 along with computed values of OA, UA, PA and K-coefficient.

Table 3. Accuracy assessment results and confusion matrix of MLC classification of original LISS-IV data. OA-overall accuracy, UA-users accuracy, PA-producers accuracy, CE-Commission Error, OE-Omission Error and K- Kappa Coefficient

From the Table 3 it may be seen that the MLC method gives satisfactory values of overall accuracy (83.15%) and kappa (k) 0.77. The minimum value of accuracy was 60.53% for the bare soil class. Similarly corresponding to dense vegetation class, the value of accuracy was low (63.24%). The residential regions (71.02%), river sand (86.97%) and road (81.25%) classes were classified with better accuracy. The reason behind the low accuracy may be the spectral confusion between these classes.

In similar manner, original hyperspectral image was also used for classification using the MLC method. The thematic map of hyperspectral data used in the MLC is shown in Fig. 10. It can be seen from the Table 4 that the results were not found to be satisfactory as compared to corresponding results obtained through LISS-IV image.

Fig. 10

MLC classification output layer of original Hyperion image

Table 4. Accuracy assessment results and confusion matrix of MLC classification of original Hyperion data. OA-overall accuracy, UA-users accuracy, PA-producers accuracy, CE-Commission Error, OE-Omission Error and K- Kappa Coefficient

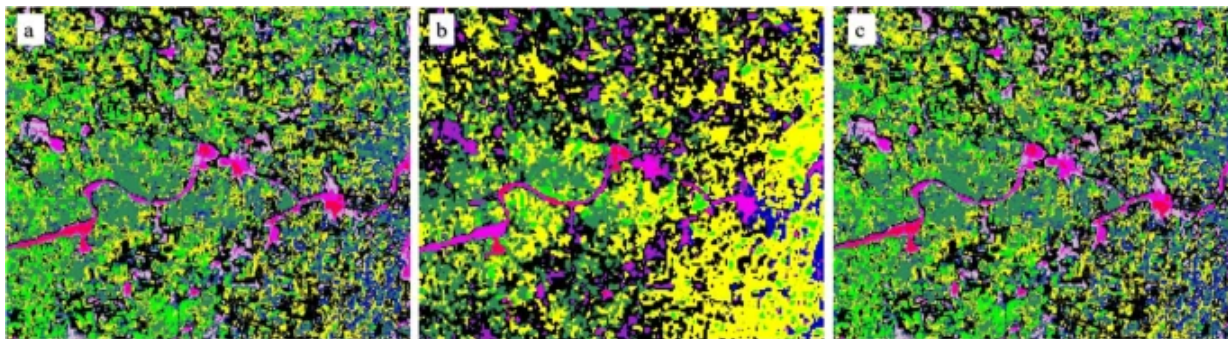
The Table 4 highlights, the spectral confusion between roads and residential regions. The lowest producer's accuracy was 0% for water class due to misclassification of water with sparse vegetations. Whereas, second lowest accuracy for the class of residential region was (32.76%) and roads (50.00%).

The overall accuracy for the classified original Hyperion data was 69.25% and kappa coefficient was 0.63 which is not satisfactory.

Similar computations have been done through fusion images obtained through fusion methods using CNSS, GST and PCSST techniques applied on Hyperion and LISS-IV images.

The Fig.11 gives illustrations of output thematic maps generated by MLC classification method on CNSS, GST and PCSST fused images. It can be seen from the Figs.11a–c that each class is classified in satisfactory manner. However, water class is identified and classified by all the three methods. The more validation was done by accuracy assessment and confusion matrix results. The Table 5 gives detail classification results for all objects, whereas the Table 6 gives values of accuracy assessment results.

Fig. 11



MLC classification output layers of fused (a) CNSS, (b) GST and (c) PCSST images respectively

Table 5 Confusion matrix of MLC classification results (in %) obtained using CNSS, PCSST and GST fused data

Table 6 Comparison of overall accuracy of MLC classification results using fused LISS-IV and Hyperion data

The producer's accuracy for the class of residential regions, dense and sparse vegetations, bare soil and water was 100% using CNSS fused image. PCSST fused image have produced very low PA for water class, moderate PA for river sand and black soil. Similarly, water class has given very less PA for GST fused image and river sand. Hence, river sand and water class misclassified with residential and vegetation classes respectively. The overall performance of the MLC classification for CNSS, PCSST and GST fused images were 94.55, 87.34 and 83.87% with 0.93, 0.83 and 0.80 kappa coefficients respectively.

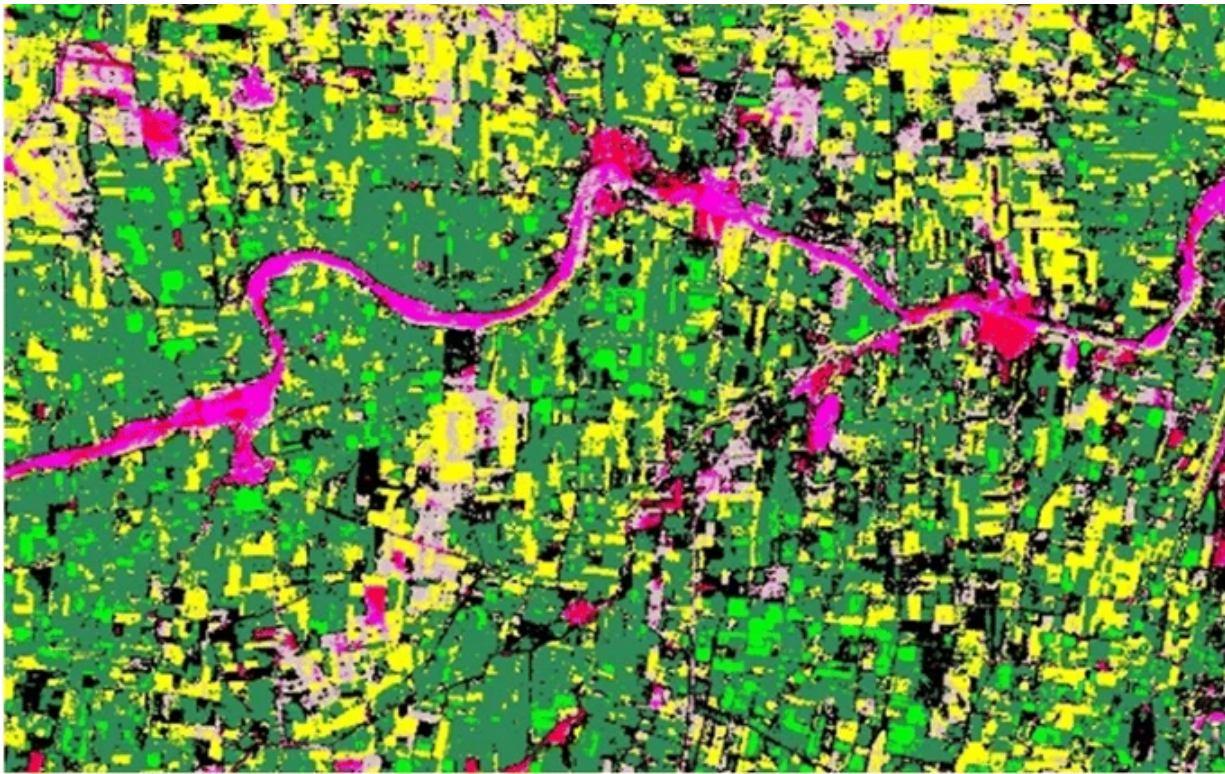
The results indicate that compared with original hyperspectral data, the CNSS fused data improved overall accuracy by 25% (69.25 to 94.55%) compared with MLC based classification. The CNSS fused data improved overall accuracy by 11% (83.87 to 94.55%) and 7% (87.34 to 94.55%) compared with GST and PCSST fused images respectively. The overall accuracy (94.55%) of our proposed approach was better than the accuracy (87.95%) of authors [1] and the accuracy (91.1%) as reported earlier [28] with MLC method. Thus, the MLC classification based on CNSS fused image performed very well as compared to GST fused image.

5.5 Results of SVM based classification

The SVM classifier can be carried out with four kernels viz. linear, polynomial, radial basis and sigmoid functions [29]. In the present study, Gaussian RBF kernel was used for conducting the SVM based classification. The reason behind the use of RBF kernel is because of its better performance and simplicity [38]. Moreover, the rest of the kernels of SVM technique was also implemented and tested on original images. The accuracy and classification results were found to be not satisfactory. Therefore it was decided to use only RBF kernel. The gamma value in RBF kernel function was set as 0.33, penalty parameter was selected to its highest value i.e. 100 to reduce the misclassification during the training [29], and pyramid level was selected as first. Pyramid reclassification threshold was selected to be 0.90 with classification probability threshold 0.20. The Fig. 12 shows the output map of original multispectral image classified by SVM method. The training pixels were selected as per the standard and each class was satisfactorily classified.

Fig. 12





SVM classification output layer of original LISS-IV image

The Table 7 contains values of the PA, UA, OA and Kappa coefficient of SVM based classification results from original multispectral image. The overall accuracy and its kappa value (86.20% and 0.82) were good as compared to MLC method for LISS-IV data.

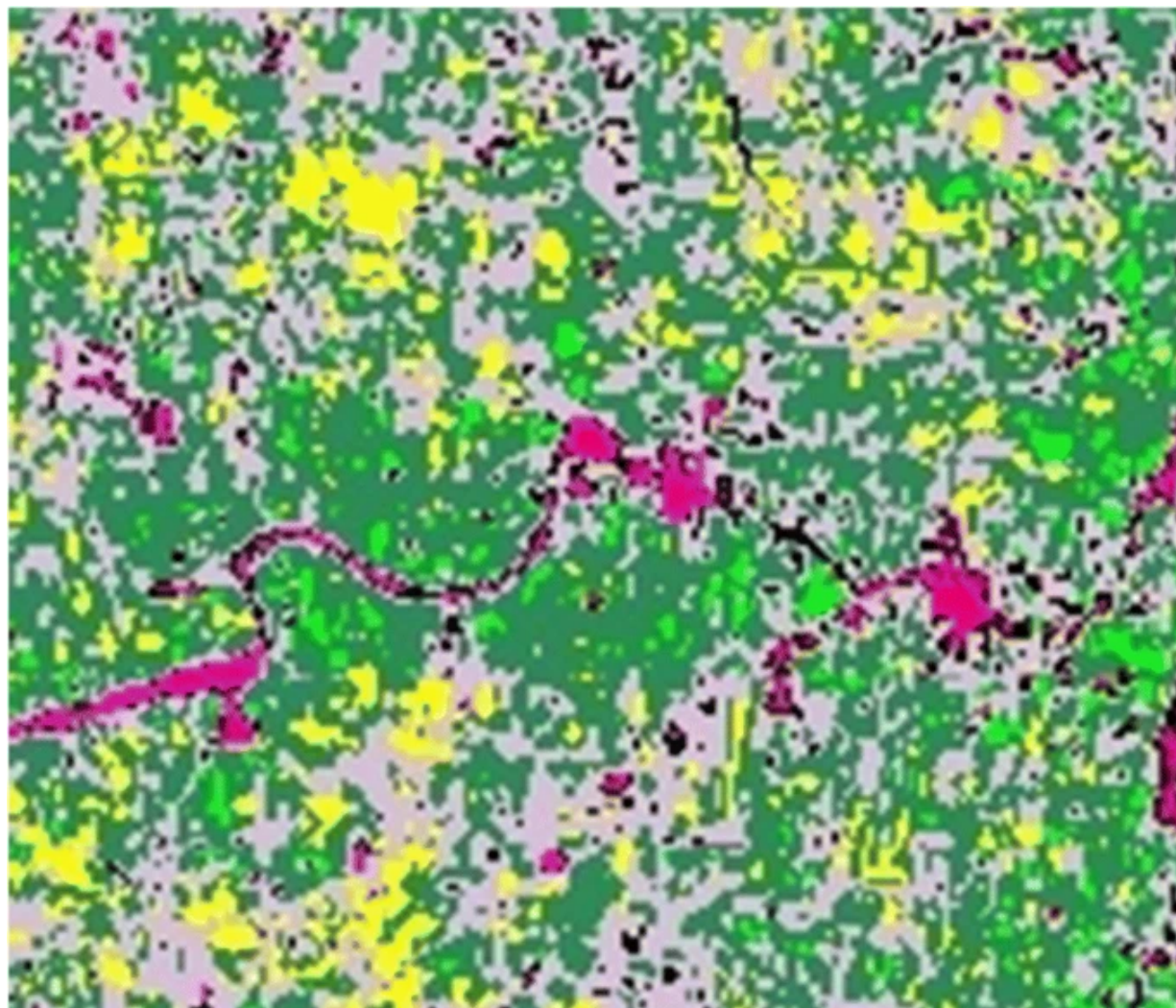
Table 7 Accuracy assessment results and confusion matrix of SVM classification of original LISS-IV data. OA-overall accuracy, UA-users accuracy, PA-producers accuracy, CE-Commission Error, OE-Omission Error and K- Kappa Coefficient

The accuracy for the bare soil and dense vegetation classes were 63.16% and 66.18% respectively. Corresponding values for the water (100%), sparse vegetation (98.35%) and black soil (99.16) were very good.

In addition, the original hyperspectral image was also classified by SVM approach (Fig. 13). The confusion matrix and classification accuracy of original Hyperion image is given in Table 8. The overall accuracy of original Hyperion based on SVM classifier produced 74.44% with kappa coefficient 0.69.

Classifications of bare soil and black soil were found to be not satisfactory here also, so same for sparse vegetation.

Fig. 13



SVM classification output layer of original Hyperion image

Table 8. Accuracy assessment results and confusion matrix of SVM classification of original Hyperion data. OA-overall accuracy, UA-users accuracy, PA-producers accuracy, CE-Commission Error, OE-Omission Error and K- Kappa Coefficient

From the Fig. [13](#) and Table [8](#), it can be seen that overall classifications were not satisfactory. The value

corresponding to water class was found to be 0 % due to unavailability of water in March, 2015 in the study area. Hence, the water body seems like residential region or roads. Moreover, the spatial structure, spectral characteristics, and color of the said classes were similar, so unable to do proper classification (Fig. 13 and Table 8). To overcome the limitations of using only single hyperspectral data, proposed fusion approach was applied on the Hyperion and LISS-IV data. The multispectral data was of February, 2014 and hyperspectral data of March, 2015. When fusion was performed, some of the multispectral classes were mixed with the hyperspectral data i.e. water class. The classified thematic maps of fused data by CNSS, GST and PCSST based SVM classifier are given in Fig. 14.

Fig. 14



SVM classification output layers of fused (a) CNSS, (b) GST and (c) PCSST images respectively

After performing fusion, PCSST algorithm generated accurate results for each class (Fig. 14c). Alternatively, CNSS and GST methods have given slightly related spectral information for each class. However, water class does not provide well with both methods (Fig. 14a and b). The confusion matrix of three methods is detailed in Table 9. The class-specific validation was carried out through accuracy assessment and confusion matrix. The dense vegetations and black soils were accurately classified for all the three fused methods using SVM algorithm. The class of residential region, river sand, bare soil and water was produced alike to each other with good accuracies. Yet, sparse vegetations were misclassified with roads. The overall accuracy of classification with SVM method based on these three fusion algorithms was calculated with its appropriate kappa statistics. The Table 10 highlighted the overall accuracy and kappa values of SVM based classification on fused images.

Table 9 Confusion matrix of SVM classification results (in %) obtained using CNSS, PCSST and GST fused data

Table 10 Comparison of overall accuracy of SVM classification results using fused LISS-IV and Hyperion data

The overall accuracy of CNSS, PCSST and GST fused approaches were 97.65%, 97.47% and 96.30 and kappa values were 0.97, 0.96 and 0.95 respectively. It was observed that, the classification accuracy by pixel based SVM method was found to be 97.65% which is better than the results (77.33% for land cover) reported earlier [42]. Similarly, the accuracy was 97.65% better as compared to results achieved by [9] for urban land cover areas.

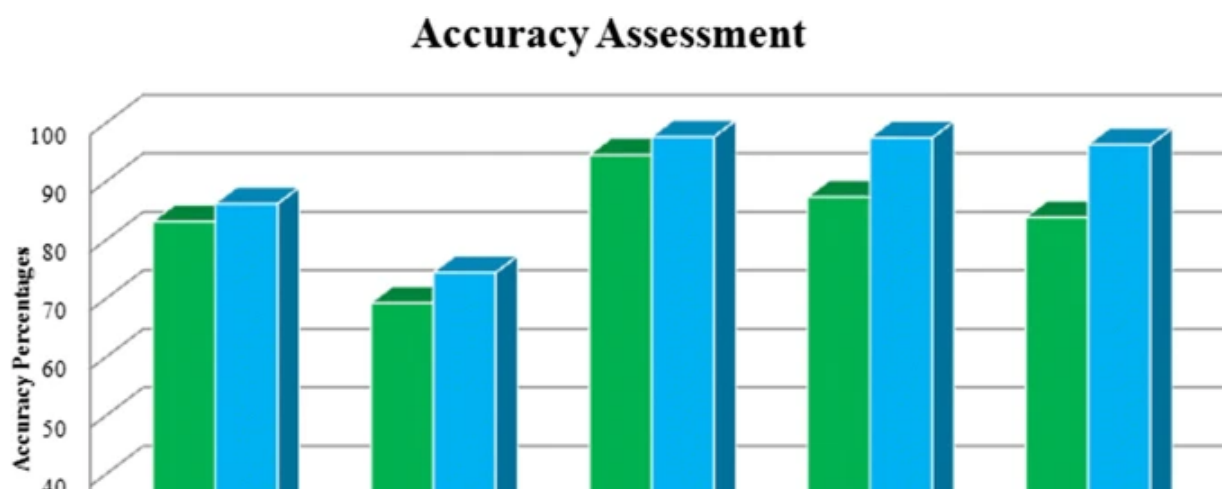
The overall accuracy given in reference [9] was reported to be as 90.30% whereas the Table 10 corresponding to the present work shows higher accuracy. The CNSS fused image enhanced overall accuracy by about 23% (74.44 to 97.65%) compared with the SVM algorithm. Further discussions about these results are given in the next section.

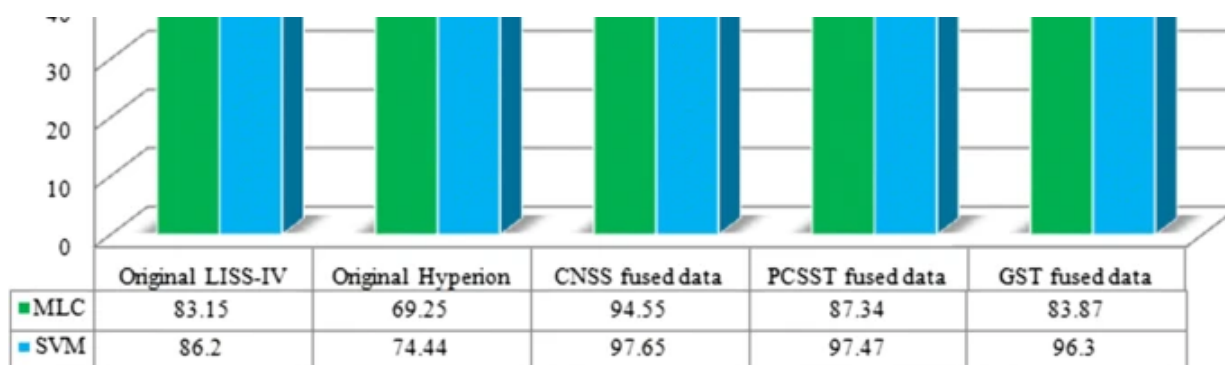
5.6 Discussions

5.6.1 The comparison and performance of MLC and SVM algorithms on original and fused data

When we applied SVM and MLC methods on original images the accuracy was not found to be satisfactory (See Fig. 15). It was found that by using fused images it was enhanced by more than 10 and 20%. The results of overall accuracy are summarized in Fig.15. It can be seen very easily that in all cases the SVM method found to be superior as compare to the MLC method when applied to five different types of images.

Fig. 15

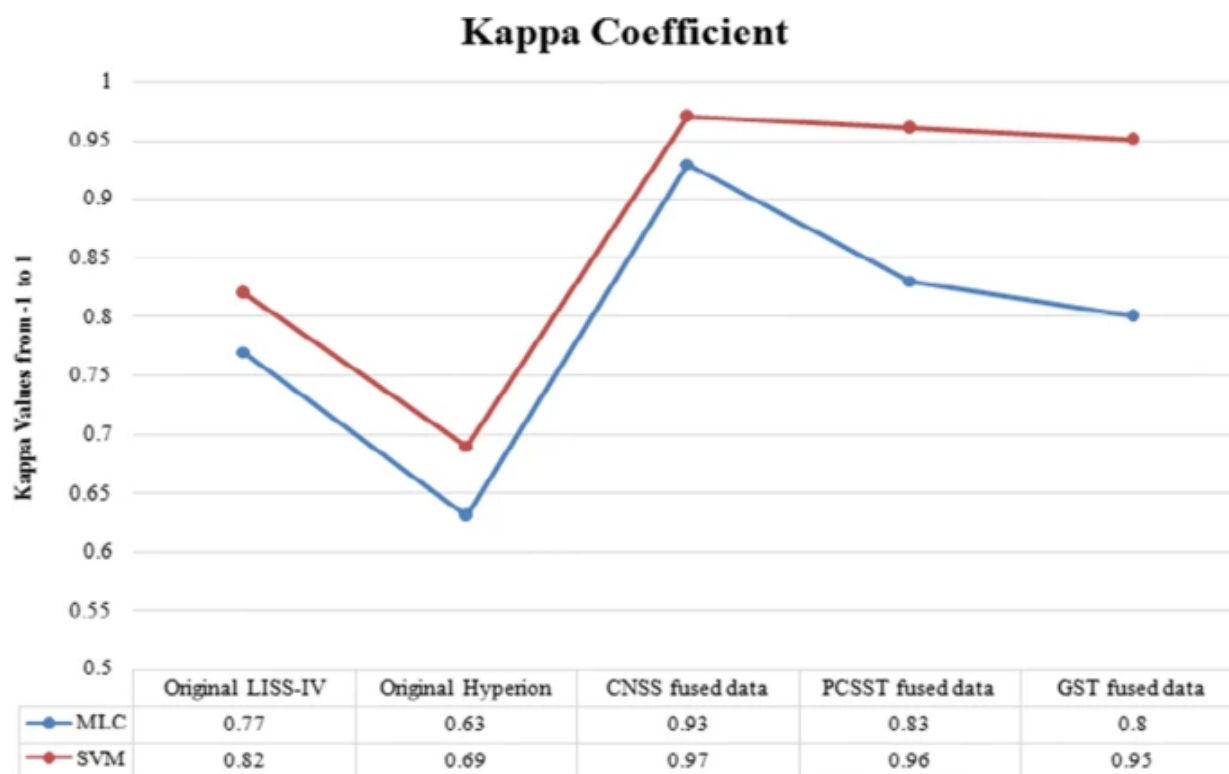




Comparison of overall accuracies for MLC and SVM classification results

The original LISS-IV data is found to be superior to the original Hyperion data. It is possible to enhance accuracy by about 3 to 5%. It can also be seen that the fusion images as extracted from LISS-IV and Hyperion are found to be better than the original two images. The fusion improves accuracy significantly about by order of 15 to 20%. The values of kappa coefficients given in the Fig.16 show similar trend.

Fig. 16



Comparison of kappa values for MLC and SVM classification results

Nevertheless, the spectral confusion between residential regions, river sands and roads is common as these class spectra are related to each other. Similarly, road class normally misclassified due to overlapping of some other classes namely bare soil, residential region or river sand. Moreover, the spectral behavior of road class is similar to bare soil, buildings and river sand. Additionally, the size, shape, structure and tone of the road class are alike to the said classes which caused the misclassification. Furthermore, the black soil and bare soil is also having alike spectral information, accordingly, confusion was increased. Similarly, spectral information of dense and sparse vegetations is also related to each other.

Overall, both the satellite datasets were acquired on different date, month and year which causes the error for some classes like water, soil and vegetations as these classes vary according to time. Nonetheless, the field campaign, user knowledge of ground objects as well as satellite data produced better training samples for the data. Furthermore, reference data was suitable and Google map and Google earth was used for validation of the identified objects.

It was found from the above results that the classes were successfully identified. However, more features may be aimed to be identifying from the residential region due the availability of various patterns in these areas. For this very high spatial resolution (less than 1 m) image is essential for the detection of fine details of urban features. Since, the images (LISS-IV and Hyperion) were of 5.8 m and 30 m spatial resolution which is not good enough to identify fine details. Consequently, we considered residential region as one of the class which includes buildings, barren lands, parking's and other urban features. In some cases, some classes were misclassified due to spectral and spatial similarities in patterns. Other superior classification techniques like neural network, decision tree classifier, knowledge-based or expert system classification with the use of ancillary data (such as DEM, topography, soil maps, census data and existing GIS-based maps) may be helpful in extracting and classifying minute details (or misclassified classes) [26].

6 Conclusions and future scope

The contribution of the present study is to propose and implement novel fusion approach using Hyperion and LISS-IV data. As per our knowledge, the proposed methodology is novel and only few studies have worked on fusion of hyper and multispectral image for classification of complex environments.

In this work, fusion images using three different techniques (CNSS, PCSST and GST) were generated by using two original satellite data, viz. the Hyperion and LISS-IV images corresponding to the AOI.

These three fusion images along with two original images have been used to get information about the AOI. Objects on the AOI were classified in eight classes and suitable field data have also been acquired for all classes. The classification techniques, viz. MLC and SVM have been used to extract information about in the AOI. This study has enabled us to get following findings:

- 1) The original Hyperion and LISS-IV image classification based on MLC classifier produced moderate classification accuracy, whereas SVM classifier produced better results with better accuracy.
- 2) The fusion of both the datasets enhanced the overall accuracy by 25% from 69.25 to 94.55% for MLC classification method. On the other side, SVM was highly increased the accuracy by 23% from 74.44 to 97.65%.
- 3) Overall, the class-specific accuracy and total accuracy was quite better with SVM approach as compared to MLC technique for LISS-IV data, Hyperion data, CNSS, PCSST and GST fused datasets.
- 4) The class-specific accuracies were also enhanced with SVM method for all the datasets as compared to the MLC.
- 5) The CNSS fusion algorithm was acceptable for both the classification methods due to its best performance with 94.55% and 97.65% overall accuracy.
- 6) It is concluded that, all the three fusion methods were performed as per the fusion algorithm expectations. The hyperspectral image has produced its spatial features after its fusion with multispectral image. Therefore, the spectral and spatial information was jointly extracted from the fused images and it is confirmed with classification accuracy results.
- 7) The present research will be valuable for better land management and its planning as well for decision making of land and its objects. In addition, this research will be the case study for other worldwide researchers for implementing similar type of study for other regions with hyperspectral and multispectral images for the classification of mixed features.

In the future work, the LiDAR data, hyperspectral data, multispectral and PAN data will be used for fusion for classification of more complex area. Moreover, the efficiency of the fusion methods will be checked and validated. In future, more superior techniques like neural network, genetic based algorithm etc. may also be used for the study.

References

1. Abbasi B, Arefi H, Bigdeli B, Motagh M, Roessner S (2015) Fusion of hyperspectral and LiDAR data based on dimension reduction and maximum likelihood. *The international archives of photogrammetry, remote sensing and spatial information sciences* 40(7):569

[Article](#) [Google Scholar](#)

2. Andrejchenko V, Liao W, Philips W, Scheunders P (2019) Decision fusion framework for Hyperspectral image classification based on Markov and conditional random fields. *Remote Sens* 11(6):624

[Article](#) [Google Scholar](#)

3. Ashraf S, Brabyn L, Hicks BJ (2012) Image data fusion for the remote sensing of freshwater environments. *Appl Geogr* 32(2):619–628

[Article](#) [Google Scholar](#)

4. E. Basaeed, H. Bhaskar and M. Al-Mualla, "comparative analysis of pan-sharpening techniques on DubaiSat-1 images," proceedings of the 16th international conference on information fusion, Istanbul, 2013, pp. 227-234. URL: <https://ieeexplore.ieee.org/document/6641282>.

5. Benediktsson JA, Pesaresi M, Amason K (2003) Classification and feature extraction for remote sensing images from urban areas based on morphological transformations. *IEEE Trans Geosci Remote Sens* 41(9):1940–1949

[Article](#) [Google Scholar](#)

6. Benediktsson JA, Palmason JA, Sveinsson JR (2005) Classification of hyperspectral data from urban areas based on extended morphological profiles. *IEEE Trans Geosci Remote Sens* 43(3):480–491

[Article](#) [Google Scholar](#)

7. Chouinard, P., & Kerekes, J. (2006, July). Decision fusion of hyperspectral and SAR data for traffic ability assessment. In 2006 IEEE international symposium on geoscience and remote sensing (pp. 2313-2316). IEEE URL: <http://ieeexplore.ieee.org/stamp/stamp.jsp?>

[tp=&arnumber=4241745&isnumber=4241146.](#)

8. Dalponte M, Bruzzone L, Gianelle D (2008) Fusion of hyperspectral and LIDAR remote sensing data for classification of complex forest areas. *IEEE Trans Geosci Remote Sens* 46(5):1416–1427
[Article](#) [Google Scholar](#)

9. Debes C, Merentitis A, Heremans R, Hahn J, Frangiadakis N, van Kasteren T, Philips W (2014) Hyperspectral and LiDAR data fusion: outcome of the 2013 GRSS data fusion contest. *IEEE Journal of Selected Topics in Applied Earth Observations and Remote Sensing* 7(6):2405–2418
[Article](#) [Google Scholar](#)

10. Dhumal R. K. et al. (2019). A spatial and spectral feature based approach for classification of crops using techniques based on GLCM and SVM. In: Panda G., Satapathy S., Biswal B., Bansal R. (eds) *Microelectronics, electromagnetics and telecommunications. Lecture notes in electrical engineering*, vol 521. Springer, Singapore. DOI: https://doi.org/10.1007/978-981-13-1906-8_5.

11. Ehlers M, Klonus S, Johan Åstrand P, Rosso P (2010) Multi-sensor image fusion for pansharpening in remote sensing. *Int J Image Data Fusion* 1(1):25–45
[Article](#) [Google Scholar](#)

12. Fauvel M, Benediktsson JA, Chanussot J, Sveinsson JR (2008) Spectral and spatial classification of hyperspectral data using SVMs and morphological profiles. *IEEE Trans Geosci Remote Sens* 46(11):3804–3814
[Article](#) [Google Scholar](#)

13. Gao, J. (2008). *Digital analysis of remotely sensed imagery*. McGraw-Hill Professional.

14. Heras DB, Argüello F, Quesada-Barriuso P (2014) Exploring ELM-based spatial–spectral classification of hyperspectral images. *Int J Remote Sens* 35(2):401–423

[Article](#) [Google Scholar](#)

15. Hsu SM, Burke HH (2003) Multi sensor fusion with hyperspectral imaging data: detection and classification. *The Lincoln Laboratory journal* 14(1):145–159 <https://archive.ll.mit.edu/publications/journal/journalarchives14-1.html>

[Google Scholar](#)

16. http://bhuvan.nrsc.gov.in/bhuvan/PDF/Resourcesat-1_Handbook.pdf. Accessed on 12 December, 2014.

17. <https://earthexplorer.usgs.gov/>. Accessed on 15 April 2015.

18. <https://www.harrisgeospatial.com/docs/cnspectralsharpening.html> Accessed on 23 April 2018.

19. <https://www.harrisgeospatial.com/docs/gramschmidtspectralsharpening.html> Accessed on 23 April 2018.

20. <https://www.harrisgeospatial.com/docs/pcspectralsharpening.html> Accessed on 23 April 2018.

21. <https://www.harrisgeospatial.com/docs/regionofinteresttool.html>. Accessed on 23 April 2018.

22. John A. Richards, “remote sensing digital image analysis”, Springer-Verlag, Berlin Heidelberg, 2013. DOI: <https://doi.org/10.1007/978-3-642-30062-2>.

23. N. Kosaka, T. Akiyama, Bien Tsai and T. Kojima, "Forest type classification using data fusion of multispectral and PAN high-resolution satellite imageries," proceedings. 2005 IEEE international geoscience and remote sensing symposium, 2005. IGARSS '05., Seoul, 2005, pp. 2980–2983. URL: <http://ieeexplore.ieee.org/stamp/stamp.jsp?tp=&arnumber=1525695&isnumber=32598>.

24. Kumar U, Milesi C, Nemani RR, Basu S (2015) Multi-sensor multi-resolution image fusion for improved vegetation and urban area classification. The international archives of photogrammetry. remote sensing and spatial information sciences 40(7):51

[Google Scholar](#)

25. Lillesand, T., Kiefer, R. W., & Chipman, J. (2014). Remote sensing and image interpretation. John Wiley & Sons.

26. Lu D, Weng Q (2007) A survey of image classification methods and techniques for improving classification performance. Int J Remote Sens 28(5):823–870

[Article](#) [Google Scholar](#)

27. Luo G, Chen G, Tian L, Qin K, Qian SE (2016) Minimum noise fraction versus principal component analysis as a preprocessing step for hyperspectral imagery denoising. Can J Remote Sens 42(2):106–116

[Article](#) [Google Scholar](#)

28. Man Q, Dong P, Guo H (2015) Pixel-and feature-level fusion of hyperspectral and LiDAR data for urban land-use classification. Int J Remote Sens 36(6):1618–1644

[Article](#) [Google Scholar](#)

29. Petropoulos GP, Arvanitis K, Sigrimis N (2012) Hyperion hyperspectral imagery analysis combined with machine learning classifiers for land use/cover mapping. *Expert Syst Appl* 39(3):3800–3809

[Article](#) [Google Scholar](#)

30. Rajput UK, Ghosh SK, Kumar A (2017) Comparison of fusion techniques for very high resolution data for extraction of urban land-cover. *Journal of the Indian Society of Remote Sensing* 45(4):709–724

[Article](#) [Google Scholar](#)

31. Saravanan, S., Jegankumar, R., Selvaraj, A., Jennifer, J. J., & Parthasarathy, K. S. S. (2019). Utility of landsat data for assessing mangrove degradation in Muthupet lagoon, South India. In coastal zone management (pp. 471–484). Elsevier.

32. Sun J, Yang J, Zhang C, Yun W, Qu J (2013) Automatic remotely sensed image classification in a grid environment based on the maximum likelihood method. *Math Comput Model* 58(3–4):573–581

[Article](#) [Google Scholar](#)

33. Swatantran A, Dubayah R, Roberts D, Hofton M, Blair JB (2011) Mapping biomass and stress in the Sierra Nevada using LiDAR and hyperspectral data fusion. *Remote Sens Environ* 115(11):2917–2930

[Article](#) [Google Scholar](#)

34. Tsagaris V, Anastassopoulos V (2005) Multispectral image fusion for improved RGB representation based on perceptual attributes. *Int J Remote Sens* 26(15):3241–3254

[Article](#) [Google Scholar](#)

35. A. D. Vibhute, K. V. Kale, R. K. Dhumal and S. C. Mehrotra, "Hyperspectral imaging data atmospheric correction challenges and solutions using QUAC and FLAASH algorithms," 2015 international conference on Man and machine interfacing (MAMI), Bhubaneswar, 2015, pp. 1–6.

URL: <http://ieeexplore.ieee.org/stamp/stamp.jsp?tp=&arnumber=7456604&isnumber=7456527>.

36. Vibhute A. D., Dhumal R. K., Nagne A. D., Rajendra Y. D., Kale K. V., Mehrotra S. C. (2016) Analysis, classification, and estimation of pattern for land of Aurangabad region using high-resolution satellite image. In: Satapathy S., Raju K., Mandal J., Bhateja V. (eds) Proceedings of the second international conference on computer and communication technologies. Advances in intelligent systems and computing, vol 380. Springer, New Delhi. DOI: https://doi.org/10.1007/978-81-322-2523-2_40.
37. Vibhute A. D. et al. (2019). Hyperspectral and Multispectral Remote Sensing Data Fusion for Classification of Complex-Mixed Land Features Using SVM. In: Santosh K., Hegadi R. (eds) Recent Trends in Image Processing and Pattern Recognition. RTIP2R 2018. Communications in Computer and Information Science, vol 1035. Springer, Singapore DOI: https://doi.org/10.1007/978-981-13-9181-1_31.
38. Widjaja E, Zheng W, Huang Z (2008) Classification of colonic tissues using near-infrared Raman spectroscopy and support vector machines. Int J Oncol 32(3):653–662
[Google Scholar](#)
39. Yang B, Cao C, Xing Y, Li X (2015) Automatic classification of remote sensing images using multiple classifier systems. Math Probl Eng 2015:1–10
[Google Scholar](#)
40. Yiqiang G, Yanbin W, Zhengshan J, Jun W, Luyan Z (2010) Remote sensing image classification by the Chaos genetic algorithm in monitoring land use changes. Math Comput Model 51(11–12):1408–1416
[Article](#) [Google Scholar](#)

41. Zhu X, Li N, Pan Y (2019) Optimization performance comparison of three different group intelligence algorithms on a SVM for hyperspectral imagery classification. *Remote Sens* 11(6):734

[Article](#) [Google Scholar](#)

42. Zoleikani R, Zoj MV, Mokhtarzadeh M (2017) Comparison of pixel and object oriented based classification of hyperspectral pansharpened images. *Journal of the Indian Society of Remote Sensing* 45(1):25–33

[Article](#) [Google Scholar](#)

Acknowledgements

The authors would like to thanks to the United States Geological Survey (USGS) for providing EO-1 Hyperion Data for this study. The authors would also like to thanks to UGC for providing BSR fellowship and lab facilities under UGC SAP (II) DRS Phase-I F.No.-3-42/2009, Phase-II 4-15/2015/DRS-II for this study. The authors would like to thank the Editor-in-Chief, the Associate Editor, managing and handling editors of MTAP and anonymous reviewers for their valuable suggestions and comments, which improved the quality of this manuscript.

Author information

Authors and Affiliations

School of Computational Sciences, Punyashlok Ahilyadevi Holkar Solapur University, Solapur, MS, 413255, India

Amol D. Vibhute & Rajesh K. Dhumal

Department of Computer Science and IT, Dr. Babasaheb Ambedkar Marathwada University, Aurangabad, MS, 431004, India

Karbhari V. Kale, Sandeep V. Gaikwad, Amarsinh B. Varpe, Dhananjay B. Nalawade & Suresh C. Mehrotra

Dr. G.Y. Pathrikar College of Computer Science and Information Technology, M G M, Aurangabad, MS, India

Ajay D. Nagne

Corresponding author

Correspondence to [Amol D. Vibhute](#).

Additional information

Publisher's note

Springer Nature remains neutral with regard to jurisdictional claims in published maps and institutional affiliations.

Rights and permissions

[Reprints and permissions](#)

About this article

Cite this article

Vibhute, A.D., Kale, K.V., Gaikwad, S.V. *et al.* Classification of complex environments using pixel level fusion of satellite data. *Multimed Tools Appl* 79, 34737–34769 (2020). <https://doi.org/10.1007/s11042-020-08978-4>

Received

13 May 2019

Revised

13 April 2020

Accepted

22 April 2020

Published

19 May 2020

Issue Date

December 2020

DOI

<https://doi.org/10.1007/s11042-020-08978-4>

Share this article

Anyone you share the following link with will be able to read this content:

[Get shareable link](#)

Provided by the Springer Nature SharedIt content-sharing initiative

Keywords

[Pixel level fusion](#)

[Color normalized spectral sharpening \(CNSS\)](#)

[Dimensionality reduction](#)

[Minimum noise fraction](#)

[Maximum likelihood classifier](#)

[Supervised classification](#)